Acta Materialia 207 (2021) 116684

Contents lists available at ScienceDirect

Acta Materialia

journal homepage: www.elsevier.com/locate/actamat

# Enhancing the Néel temperature in 3*d*/5*d* $R_2NiIrO_6$ (R=La, Pr and Nd) double perovskites by reducing the $R^{3+}$ ionic radii

P. Kayser[a,b,*], A. Muñoz[c], J.L. Martínez[a], F. Fauth[d], M.T. Fernández-Díaz[e], J.A. Alonso[a,*]

[a] Instituto de Ciencia de Materiales de Madrid, C.S.I.C., Cantoblanco, E-28049 Madrid, Spain
[b] Centre for Science at Extreme Conditions and School of Chemistry, The University of Edinburgh, Edinburgh EH9 3JZ, U.K
[c] Dpto. de Física Aplicada, EPS, Universidad Carlos III, Avda. Universidad 30, Leganés, 28911 Madrid, Spain
[d] CELLS – ALBA Synchrotron, 08290, Cerdanyola del Valles, Barcelona, Spain
[e] Institut Laue Langevin, BP 156X, Grenoble F-38042, France

ARTICLE INFO

*Article history:*
Received 28 June 2020
Revised 11 January 2021
Accepted 18 January 2021
Available online 21 January 2021

*Keywords:*
Iridium
Double perovskites
5d transition metals
Neutron powder diffraction
$La_2NiIrO_6$
$Pr_2NiIrO_6$
$Nd_2NiIrO_6$

ABSTRACT

Double perovskites containing $Ir^{4+}$ were synthesised by a citrate technique, followed by an annealing treatment in air at 1100 °C. The crystal structure of the three compounds, with formula $R_2NiIrO_6$ (R= La, Pr and Nd), were determined using a combined refinement against neutron powder diffraction (NPD) and synchrotron x-ray powder diffraction (SXRPD) data sets. At room temperature, all the samples were indexed in the space group $P2_1/n$ and the monoclinic symmetry remains in the 300 to 1273 K temperature range. Magnetization measurements suggest competitive antiferromagnetic and ferromagnetic interactions, with an unexpected increment of the ordering temperature ($T_N$) along the series. The magnetic structures of all the samples were defined with the propagation vector k = 0; the $Ni^{2+}$ and $Ir^{4+}$ moment arrangement, different for each compound, shows a strong dependence on the nature of the rare-earth ion.



## 1. Introduction

Iridium-based perovskites have shown to exhibit interesting and unexpected physical properties due to their particular electronic structures, arising from the spin-orbit coupling effect. In the more spatially extended 5d orbitals, the Coulomb interactions are typically weaker and its energy value is comparable to the corresponding spin-orbit coupling energy scale, leading to a modification of the electronic structure. In the perovskite structure, the 5d-orbitals of the metals located in an octahedral coordination split into $e_g$ and $t_{2g}$ levels due to the crystal electric field and, subsequently, the $t_{2g}$ triplet develops into the levels with $J_{eff}$= 3/2 and ½ due to the spin-orbit coupling effect. Since the ground state of iridium perovskites seems to be strongly modifiable, this offers a rich opportunity to tailor the physical properties of these materials.[1,2]

Rock-salt ordered double perovskites $A_2BB'O_6$ containing 3d and 5d (Ir, Re, Os) metals over the B-site have recently attracted a great deal of attention.[3] There are many examples of 3d/5d double perovskites with outstanding properties, such as as half-metals with colossal magnetoresistance ($Sr_2FeReO_6$) [4,5] or magnetic order far above room temperature ($Sr_2CrOsO_6$, $Sr_2CrReO_6$) [6,7]; however, there are just a few examples containing iridium.

In the present paper, we aim to investigate the crystal and magnetic structure of three members of the $R_2NiIrO_6$ family (R= rare earths). In these oxides, containing $Ni^{2+}$ and $Ir^{4+}$ over the B-site, the magnetic ordering temperature varies from 75 K ($La_2NiIrO_6$) to 207 K ($Lu_2NiIrO_6$) [8–14]. The common behaviour observed in double perovskites to accommodate the effect of decreasing the $R^{3+}$ size in the structure is to reduce the tilting angle Ni-O-Ir from 180 degrees, leading to more distorted structures. In general, this would worsen the orbital overlapping and therefore, the magnetic interactions. In this particular system, we have observed the opposite trend. The enhancement of the magnetic ordering temperature with the reduction of the A-site cation size is understood from the magnetic structure features, unveiling the magnetic interactions predominant in this system and how they are affected by changes in the crystal structure. This is a comprehensive study, by state-of the art techniques like neutron or synchrotron x-ray diffraction, including aspects that have been never been addressed,

* Corresponding authors.
*E-mail addresses:* paula.kayser@ed.ac.uk (P. Kayser), ja.alonso@icmm.csic.es (J.A. Alonso).

https://doi.org/10.1016/j.actamat.2021.116684
1359-6454/

like the high-temperature structural evolution until almost 1000 °C and the description of the microscopic arrangements of the low T magnetic structures.

## 2. Experimental section

Polycrystalline samples of $R_2NiIrO_6$ (R= La, Pr, Nd) were prepared by using the citrate-nitrate route. Stoichiometric amounts of $La_2O_3$ (pre-treated at 900 °C to remove carbonates and water) $Pr_6O_{11}$, $Nd_2O_3$ (Alfa Aldrich, 99.9%) and $Ni(NO_3)_3.6H_2O$ (Merck, 99.5%) were dissolved in 200 ml of citric acid aqueous solution (10% w/w); 1 ml of $HNO_3$ (68% vol) was added in order to facilitate the dissolution of the rare-earth oxides. $IrO_2$ (Strem, 99%) was not dissolved and remained in suspension under constant stirring. The solution was evaporated, resulting in an organic resin that includes a homogeneous distribution of all the cations and, subsequently, the resin was dried at 140°C. To eliminate the organic residues and the nitrates, a thermal treatment at 600°C during 12 h was applied. Once the precursors were prepared, they were annealed at 1100°C for 12 h in air.

The initial characterization of the samples and the reaction progress was followed after each treatment by X-ray diffraction (XRD) until single-phase perovskite materials were identified. A Bruker-AXS D8 diffractometer (40 kV, 30 mA), controlled by DIFFRACPLUS software, in Bragg–Brentano reflection geometry with Cu K$\alpha$ radiation ($\lambda$ = 1.5418 Å) and a position sensitive detector (PSD) were utilized. A detailed investigation of the crystal structure was carried out by means of high-angular resolution synchrotron x-ray diffraction and powder neutron diffraction. Synchrotron x-ray powder diffraction (SXRPD) experiments were performed at the BL04-MSPD beamline of ALBA synchrotron and the patterns were collected in high- angular resolution mode (so-called MAD set-up, Multicrystal Analyser Detectors), selecting an incident beam with 38 keV radiation ($\lambda$= 0.3251 Å) [15]. The samples were contained in 0.7 mm diameter quartz capillaries. Using high-energy synchrotron x-rays allowed collecting data on such absorbing materials in transmission mode. SXRPD data were recorded at 295 (RT), 673, 1073 and 1263 K to study potential phase transitions. Neutron powder diffraction (NPD) experiments were accomplished at room temperature and 3 K in the high-angular resolution D2B instrument ($\lambda$ = 1.594 Å) of the Institut Laue- Langevin (ILL) in Grenoble (France). The low-temperature data were collected to investigate the magnetic structure of the samples. All the structures were refined by the Rietveld method [16] using the Fullprof refinement software [17]. No regions were excluded in the refinement. To generate the line shape of the diffraction peaks, a pseudo-Voigt function was chosen. The following parameters were refined in the final analysis: scale factor, zero-point error, background coefficients, lattice parameters, positional coordinates, isotropic atomic displacements and magnetic moments.

The magnetic properties were analysed in a commercial Quantum-Design superconducting quantum interference device (SQUID) magnetometer in the range of 5–300 K. Direct current magnetic susceptibility was measured under zero-field cooled (ZFC) and field-cooled (FC) conditions with a magnetic field of 0.1 T. Isothermal magnetization curves were obtained for magnetic fields going from −5 T to 5 T at 4 and 300 K.

The Scanning Electron Microscopy study was carried out in a Hitachi instrument, model TM-1000, coupled to an energy-dispersive X-ray spectrometer (EDX), working with an acceleration voltage of 15 kV and 60 s of acquisition time.

## 3. Results and discussion

*Room- temperature crystal structure*. The samples were obtained as pure black and well-crystallised powders. The SXRPD and NPD

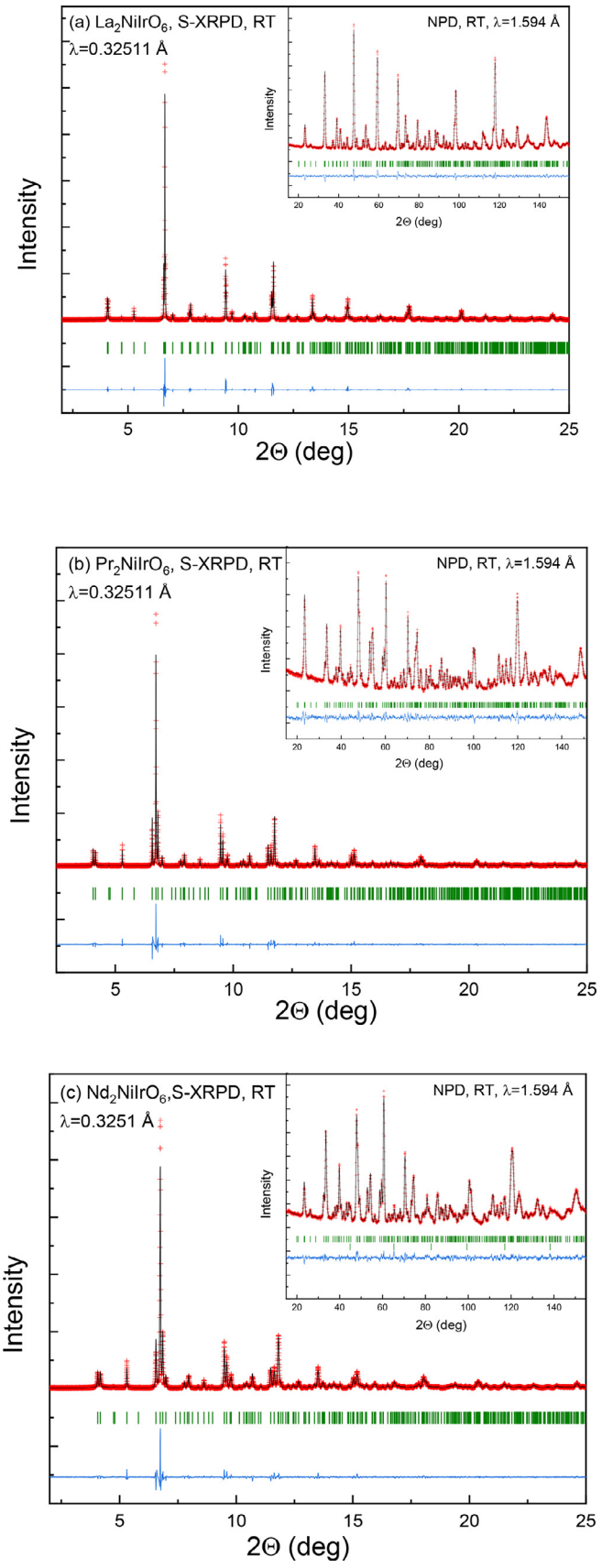


**Fig. 1.** Combined SXRPD-NPD Rietveld refinement profiles for (a) $La_2NiIrO_6$, (b) $Pr_2NiIrO_6$ and (c) $Nd_2NiIrO_6$ at room temperature. The crosses are the experimental data, the black solid line is the calculated profile, the first series of Bragg reflections correspond to the main perovskite phase ($P2_1/n$), and the second one on the $Nd_2NiIrO_6$ pattern corresponds to vanadium from the sample container.

**Table 1**
Unit-cell, positional and thermal parameters for $R_2NiIrO_6$ defined in the $P2_1/n$ (no. 14) space group, from SXRPD-NPD combined refinement at RT. Chemical composition (in weight) for the metal elements from EDX is also included, with the nominal values in parentheses.

| | $La_2NiIrO_6$ | $Pr_2NiIrO_6$ | $Nd_2NiIrO_6$ |
|---|---|---|---|
| a (Å) | 5.56657(7) | 5.47637(9) | 5.44394(11) |
| b (Å) | 5.63139(7) | 5.67944(10) | 5.68510(15) |
| c (Å) | 7.89310(12) | 7.80462(16) | 7.77770(20) |
| $\beta$ (°) | 90.036(4) | 90.022(6) | 90.027(8) |
| V (Å$^3$) | 247.429(6) | 242.745(8) | 240.71(1) |
| **$R_{4e}$ (x y z)** | | | |
| x | -0.0088(6) | -0.0127(6) | -0.0142(5) |
| y | 0.45560(15) | 0.44250(20) | 0.43843(20) |
| z | 0.2500(3) | 0.2501(3) | 0.2502(3) |
| B (Å$^2$) | 0.67(2) | 0.62(4) | 0.86(3) |
| **$Ni_{2d}$ (0 0 ½)** | | | |
| Occ $(Ni/Ir)_{2b}$ | 0.962(6)/0.038(6) | 0.908(8)/0.092(8) | 0.870(8)/0.128(8) |
| B (Å$^2$) | 0.481(3) | 1.51(9) | 1.51(9) |
| **$Ir_{2a}$ (0 0 0)** | | | |
| Occ $(Ir/Ni)_{2a}$ | 0.962(6)/0.038(6) | 0.908(8)/0.092(8) | 0.870(8)/0.128(8) |
| B (Å$^2$) | 0.13(2) | 0.13(3) | 0.12(4) |
| **$O1_{4e}$ (x y z)** | | | |
| x | 0.0834(9) | 0.0886(12) | 0.0977(10) |
| y | 0.0180(8) | 0.0286(14) | 0.0279(10) |
| z | 0.2497(19) | 0.248(2) | 0.246(2) |
| B (Å$^2$) | 0.99(7) | 1.88(11) | 1.59(9) |
| **$O2_{4e}$ (x y z)** | | | |
| x | 0.2061(16) | 0.1960(15) | 0.1930(17) |
| y | 0.2800(13) | 0.2856(14) | 0.3057(15) |
| z | -0.0483(13) | -0.0392(11) | -0.0382(11) |
| B (Å$^2$) | 0.71(16) | 0.55(16) | 0.63(16) |
| **$O3_{4e}$ (x y z)** | | | |
| x | 0.2865(15) | 0.292(2) | 0.299(2) |
| y | 0.8008(13) | 0.8034(19) | 0.7928(19) |
| z | -0.0385(12) | -0.0569(15) | -0.0584(13) |
| B (Å$^2$) | 0.21(15) | 1.7(2) | 1.4(2) |
| **Reliability Factors** | | | |
| $\chi 2$ | 2.29 | 1.66 | 1.66 |
| Rp (%) | 2.87 | 2.40 | 2.36 |
| Rwp (%) | 3.59 | 3.02 | 3.05 |
| Rexp (%) | 2.37 | 2.35 | 2.37 |
| $R_I$ (%) | 2.59 | 2.67 | 2.54 |
| **Chemical analysis (EDX)** | | | |
| R | 53.2 (52.54) | 54.8 (52.90) | 54.7 (53.48) |
| Ni | 12.0 (11.10) | 11.5 (11.02) | 12.2 (10.88) |
| Ir | 34.8 (36.35) | 33.7 (36.08) | 33.1 (35.64) |

patterns were successfully indexed in the monoclinic space group $P2_1/n$. The unit-cell parameters are related to $a_0$ (ideal cubic perovskite $a_0 \approx$ 3.8 Å) as a$\approx \sqrt{2}a_0$, b$\approx \sqrt{2}a_0$ and c$\approx 2a_0$, $\beta \approx 90°$. In this model, R atoms are located at 4*e* (x y z) positions, Ni at 2*d* (0 0 ½) positions, Ir at 2*c* (0 0 0) and the three types of oxygen atoms at 4*e* (x y z) sites. SXRPD patterns displayed sharp and well-defined reflections characteristic of a perovskite-like structure including superstructure reflections that confirm the existence of rock-salt ordering of $Ni^{2+}$ and $Ir^{4+}$. Based on the Anderson *et al* criterion [18], neither the ionic radii difference of the cations, r($Ni^{2+}$)= 0.69Å and r($Ir^{4+}$)= 0.625 Å, nor the difference in the charge is big enough to establish full 1:1 B-site ordering. However, the difference in covalency between Ir-O bonds with the less covalent Ni-O bonds, is sufficient to drive a long-range cationic ordering [19]. The results from EDX analysis showed well-defined peaks corresponding to R, Ni and Ir; the determined weight % of these elements (Table 1) is in reasonable agreement with the nominal values (in parentheses).

Fig. 1 shows the plots after a combined Rietveld refinement against SXRPD and NPD data. High-angular resolution SXRPD data are helpful to unequivocally assign the correct symmetry to the structure, whereas NPD provides essential information about the atomic coordinates of the anions. For this family of compounds, this combined method is especially appropriate to refine the crystal structure. On one side, perovskite structures with non- optimal relationship between the size of A- and B- cations undergo a cooperative tilting of the $BO_6$ octahedral network, which implies small displacements of the anions. Thus, NPD is one of the most suitable techniques to determine the atomic coordinates and the displacement factors of the oxygen atoms, which is especially challenging in compounds containing heavy metals such as iridium. On the other side, the presence of Ni and Ir over the B-sites of the perovskites, with extremely similar neutron scattering lengths, Ni (1.03 fm) and Ir (1.06 fm), prevents the refinement of the antisite disorder in the structure from NPD data, and then, SXRPD is required. Table 1 summarizes the obtained structural parameters: unit-cell parameters, volume and atomic positions. Bond distances and selected angles as well as the valence of the cations were determined with the program Bonds-Str in the Fullprof package (Table 2).

**Table 2**
Main interatomic bond distances (Å) and selected angles (deg) for $R_2NiIrO_6$, determined from the combined refinement from SXRPD-NPD data at RT. The bond-valence sums (BVS) values have also been included for Ni and Ir.

| | $La_2NiIrO_6$ | $Pr_2NiIrO_6$ | $Nd_2NiIrO_6$ |
|---|---|---|---|
| **RO polyhedra** | | | |
| R-O1 | 2.518(5) | 2.458(8) | 2.422(6) |
| R-O1 | 2.421(6) | 2.420(8) | 2.419(6) |
| R-O2 | 2.827(10) | 2.702(9) | 2.722(9) |
| R-O2 | 2.446(9) | 2.485(9) | 2.422(9) |
| R-O2 | 2.622(9) | 2.669(9) | 2.644(9) |
| R-O3 | 2.704(9) | 2.596(12) | 2.564(11) |
| R-O3 | 2.449(9) | 2.363(12) | 2.383(11) |
| R-O3 | 2.740(9) | 2.815(12) | 2.815(11) |
| **<R-O>$_{8\ short}$** | **2.591(9)** | **2.560(9)** | **2.548(8)** |
| **$NiO_6$ polyhedra** | | | |
| Ni-O1 (x2) | 2.034(15) | 2.037(15) | 2.059(15) |
| Ni-O2 (x2) | 2.102(9) | 2.135(8) | 2.087(9) |
| Ni-O3 (x2) | 2.099(8) | 2.136(11) | 2.069(11) |
| **<Ni-O>** | **2.08(1)** | **2.10(3)** | **2.07(1)** |
| $\Delta\delta$ $10^4$ | 2.28 | 4.90 | 0.32 |
| **$IrO_6$ polyhedra** | | | |
| Ir-O1 (x2) | 2.028(15) | 2.006(15) | 1.998(15) |
| Ir-O2 (x2) | 1.995(8) | 1.991(8) | 2.077(9) |
| Ir-O3 (x2) | 1.989(8) | 2.048(11) | 2.118(11) |
| **<Ir-O>** | **2.00(1)** | **2.01 (3)** | **2.06(1)** |
| $\Delta\delta$ $10^4$ | 2.02 | 1.43 | 5.88 |
| Ni-O1-Ir | 152.6(6) | 149.7(6) | 146.9(6) |
| $\phi$ | 13.7 | 15.1 | 16.5 |
| Ni-O2-Ir | 152.8(3) | 153.5(3) | 149.8(4) |
| $\phi$ | 13.6 | 13.2 | 15.1 |
| Ni-O3-Ir | 153.9(3) | 147.4(4) | 147.5(4) |
| $\phi$ | 13.0 | 16.3 | 16.3 |
| O1-Ni-O2 | 88.7(7) | 89.1(8) | 87.2(8) |
| O1-Ni-O3 | 88.2(6) | 90.0(9) | 90.0(8) |
| O2-Ni-O3 | 89.9(5) | 89.0(6) | 86.1(7) |
| O1-Ir-O2 | 89.3(7) | 86.7(8) | 85.6(8) |
| O1-Ir-O3 | 89.3(7) | 87.1(8) | 88.5(8) |
| O2-Ir-O3 | 86.8(5) | 87.6(7) | 89.4(7) |
| **BVS** | | | |
| Ni | 1.91(2) | 1.80(2) | 1.94(2) |
| Ir | 4.20(5) | 4.06(5) | 3.60(5) |

During the refinement, the occupancies of Ni and Ir sites were constrained as occ(Ni) + occ(Ir)= 1. At room temperature, all the samples show certain degree of disorder over the B-site. Anti-site disorder occurs if some Ni is located at Ir positions, and vice versa. As long as the tolerance factor, defined as $t = \frac{(r_A+r_O)}{\sqrt{2}(r_B+r_O)}$ deviates from the ideal value of 1, the percentage of anti-site degree undergoes an increment: 4% (La), 9% (Pr) and 13% (Nd). The occupancy factors of oxygen atoms have also been refined, and the results confirm a full oxygen stoichiometry for all the samples.

The present unit-cell parameters are in good agreement with formerly reported values. $La_2NiIrO_6$ was initially described using a simplified pseudocubic perovskite structure of unit-cell parameter 7.918 Å [10] but more recent works on powder (R=La [11]) and single crystals (R= Pr and Nd [12]) reported monoclinic symmetry, hence concurring with our results. The variation of the unit-cell parameters and volume are represented in Fig. 2. An increment of unit-cell volume with the ionic size is shown in the inset of Fig. 2, corresponding to a volume decrease along the lanthanides series. However, while the *a*- and *c*- axes exhibit a decrease along the series, the corresponding *b*-axis slightly elongates and then starts shortening from a critical $R^{3+}$size.[8] In $Lu_2NiIrO_6$, the reported *b* value is 5.63533(2) Å [8], which is virtually equal to the corresponding one for R=La. This effect has been previously observed in similar perovskites, such as $RVO_3$ [20] or $R_2NiRuO_6$ [21]. It is ascribed to the tilting system adopted by this family of compounds, corresponding to the $a^-a^-b^+$ in the Glazer's notation, [22] where

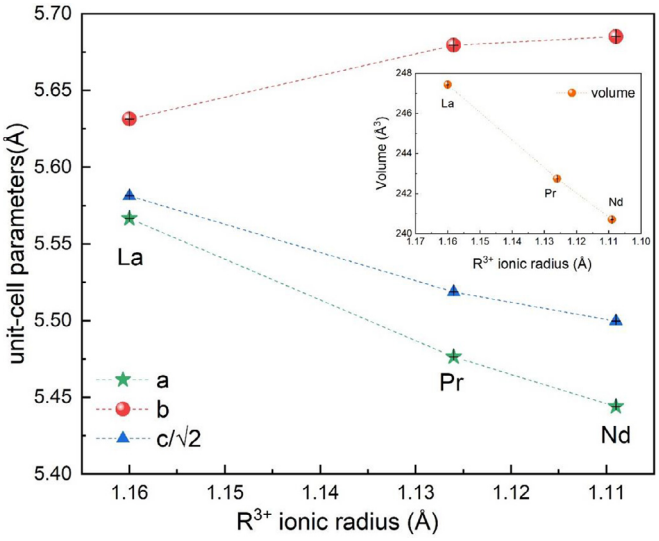


**Fig. 2.** Variation of the unit-cell parameters and volume (inset) for $R_2NiIrO_6$ perovskites (R= La, Pr and Nd) with the ionic radius of $R^{3+}$.

the structural distortion driven by the reduction of the size of the $R^{3+}$ causes minimal modifications of the *b* value. In addition, it is observed that the value $c/\sqrt{2}$ lies between *a* and *b*, which is characteristic of the so-called O structure, and it represents a common feature in the perovskites where the primary distorting effect is steric.

The local coordination of the three different cations has also been investigated. The A-site of the perovskite, occupied by rare earths ($La^{3+}$, $Pr^{3+}$, $Nd^{3+}$), is highly distorted and the effective coordination environment is reduced to a $RO_8$ polyhedron, rather than a $RO_{12}$ oxygen coordination. In the octahedral sites, the average distances <Ni-O> and <Ir-O> compare well with the calculated values obtained from the sums of Shannon [23] effective radii: of 2.09 Å for $^{VI}Ni^{2+}$ (0.690 Å)-$^{VI}O^{2-}$ and 2.025 Å for $^{VI}Ir^{4+}$(0.625 Å) -$^{VI}O^{2}$. It is observed that the average bond distances scale with the size or $R^{3+}$, while the Ni-O and Ir-O bond lengths remain constant along the series and thus, the drop of the unit-cell volume is directly related to the contraction of the $RO_8$ polyhedra.

The valences of the cations and anions, $S_{ij}$, were estimated using Sij=exp[($R_0-R_{ij}$)/B], corresponding to the Brown's Bond-Valence Model (BVS), and the following parameters: B = 0.37, $R_0(Ni^{2+})$= 1.654, and $R_0(Ir^{4+})$= 1.87, were employed for the calculation.[24] In all of the samples, the oxidation state of Ni and Ir are reasonably close to 2+ and 4+, respectively (Table 2). It is interesting the trend of the valence of Ir to progressively decrease from La to Nd perovskites, which can be understood as the basicity of the rare-earth ion decreases and, therefore, the ability to stabilize a high oxidation state of this transition metal ion is also weaker.

*Variable- temperature crystal structure.* Fig. 3 shows a portion of SXRPD patterns acquired at 673, 1073 and 1263 K (RT patterns were included for the sake of comparison) for R= La and Pr, aiming to study the thermal evolution of the crystal structure. A first visual analysis of the data suggested that there is a structural phase transition towards higher symmetries, such as tetragonal or cubic, since the peak splitting seems to vanish upon heating. However, a careful examination of the patterns revealed that, in this temperature range, all the reflections still remain. In order to identify the correct tilting system and space group, some of the reflections were indexed in the double-edge cubic cell (a= 7.9649(1) Å), at 1260 K. Subsequently, they were assigned to the corresponding R-, M- and X-point modes [25], which are associated with the rock-

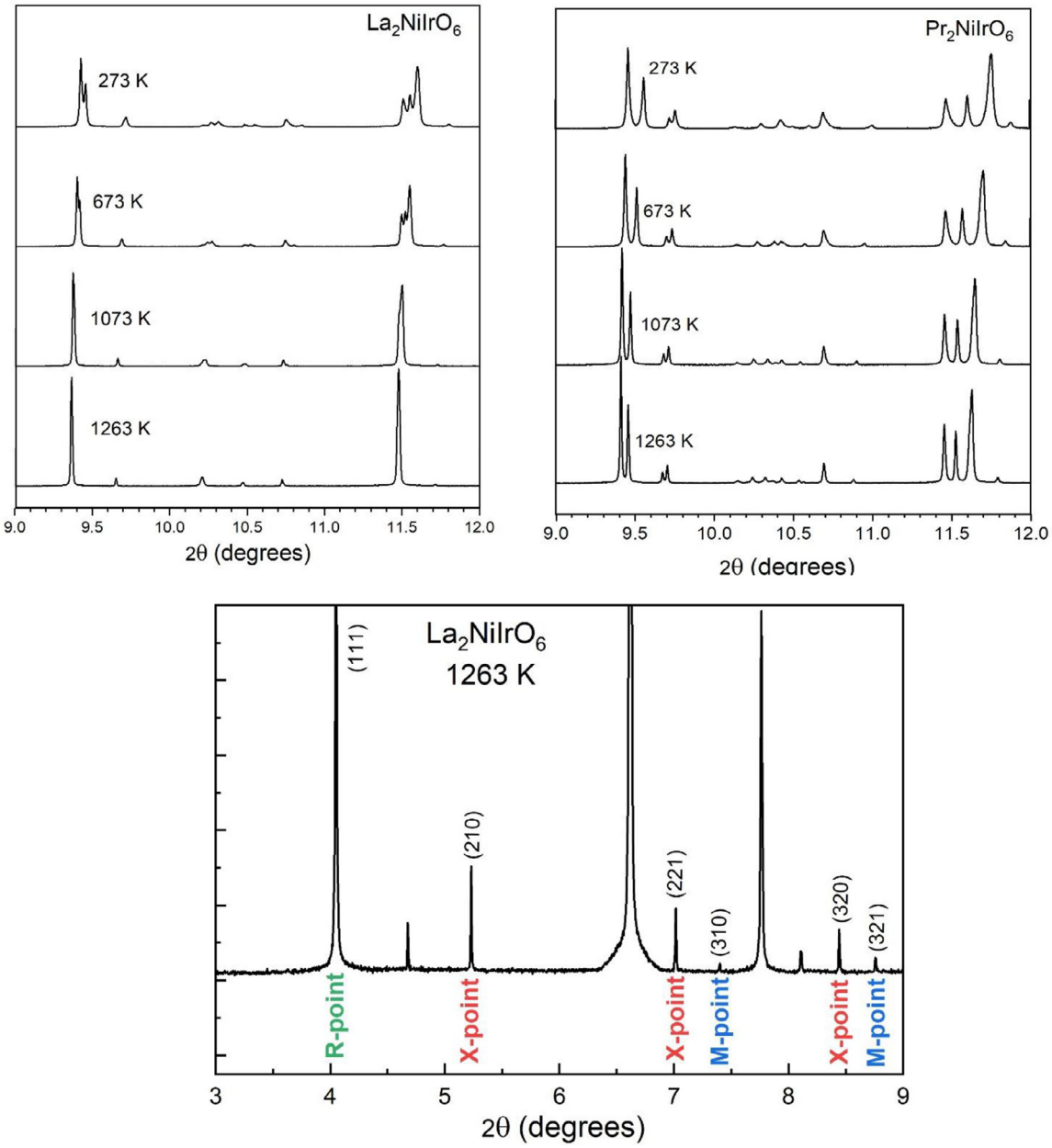


**Fig. 3.** Portions of SXRPD for $R_2NiIrO_6$ perovskites (R= La and Pr) at 298, 673, 1073 and 1263 K (top) and the SXRPD pattern for R= La highlighting superlattice reflections associated with cooperative tilting of the octahedra (bottom).

salt ordering or/and out-of-phase octahedral tilting, the in-phase octahedral tilting and to the coupling of the out-of-phase and the in-phase octahedral tilting, respectively (Fig. 3).

The relevant point in this analysis is the presence of M- and X-points. The prevalence of these diffraction peaks at high temperature suggests the same *a-a-c+* tilt system corresponding to the space group $P2_1/n$ [22,25].

It is worth commenting that the coupling of the in- and out-phase octahedral tilting provokes a displacement of the A-site cations, leading to a reduction of the coordination environment of $R^{3+}$ cations, from $RO_{12}$ to $RO_8$, as observed in the bond- distances obtained from the refinements (Table 2).

As shown in Fig. 3, the symmetry of the $Pr_2NiIrO_6$ structure remains virtually unchanged with the temperature: only a small reduction of the peak splitting is observed. While $La_2NiIrO_6$ seems to be about undergoing a phase transition at temperatures just above 1263 K, in the $Pr_2NiIrO_6$ compound no signs of phase transitions are observed. The smaller ionic radii of $Pr^{3+}$ gives rise to a more distorted structure at room temperature and requires a higher temperature range to evolve into a higher symmetry structure.

Based on the discussion above, all the variable-temperature structures were refined using the room temperature model in the space group $P2_1/n$. The goodness of the refinements is shown in Figure S1. Tables S1 and S2 summarise the refined parameters.

The thermal evolution of the lattice parameters shows the same type of behaviour than those previously observed with the $R^{3+}$ cation size. *a* and *c* unit-cell parameters evolve as expected, increasing while the temperature rises; however, the variation of *b* is negligible, with a very slight decrement. Overall, the unit cell undergoes an expansion with the temperature, as it can be observed in the evolution of the volume (inset of Fig. 4), which is strongly anisotropic. Another common feature is the observed value of $c/\sqrt{2}$, which lies between *a* and *b* along the whole range of temperatures.

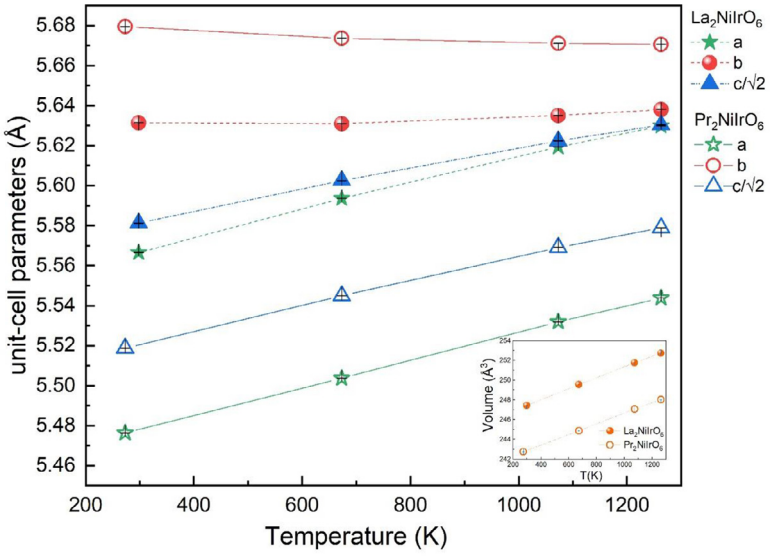


**Fig. 4.** Thermal evolution of the unit-cell parameters and volume (inset) for $R_2NiIrO_6$ perovskites (R= La and Pr). The error bars are smaller than the size of the symbols.

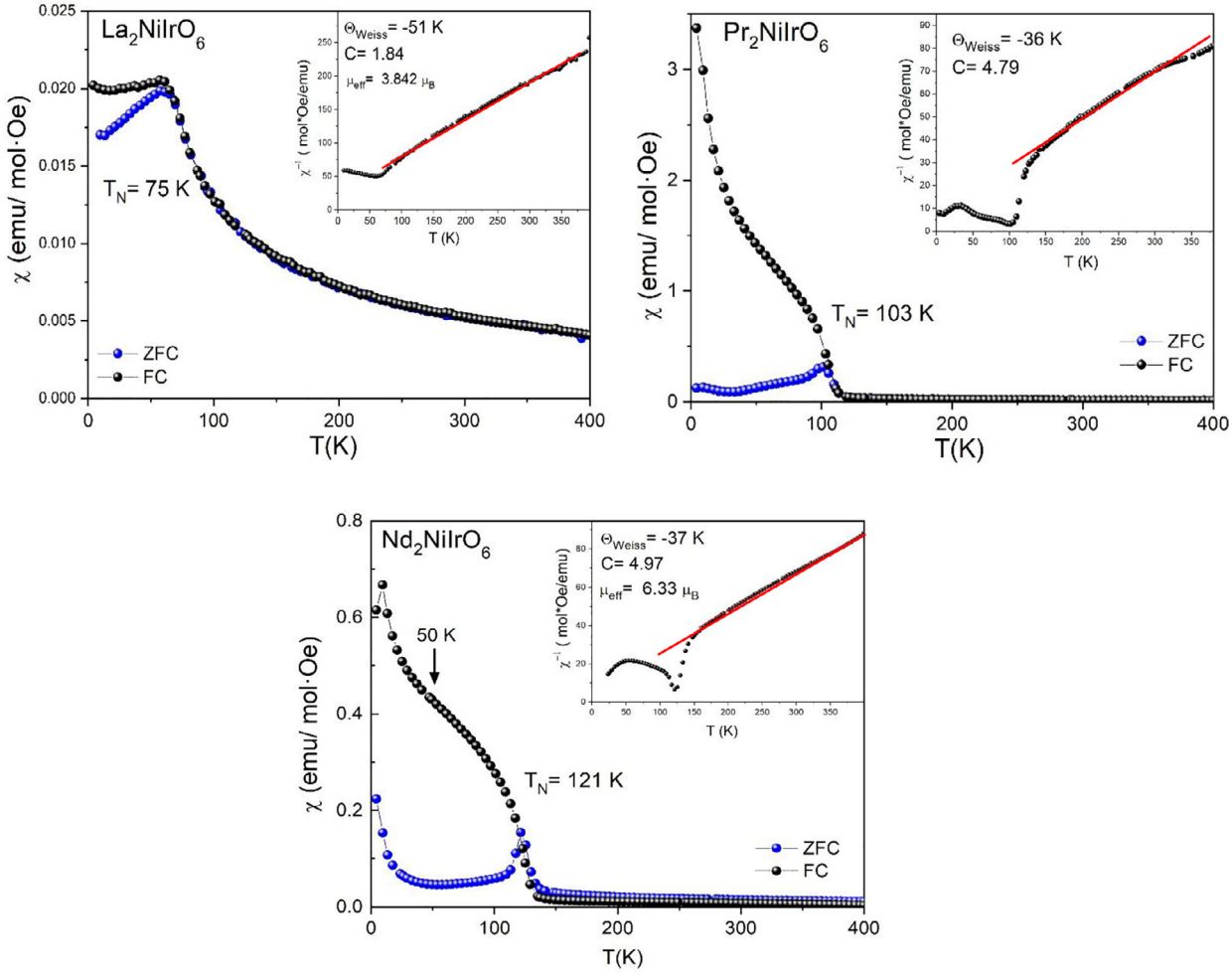


**Fig. 5.** Temperature dependence of the dc magnetic susceptibility for the $R_2NiIrO_6$ (R = La, Pr, Nd) perovskites, measured under a 0.1 T magnetic field. The inset shows the reciprocal ZFC susceptibility versus temperature.

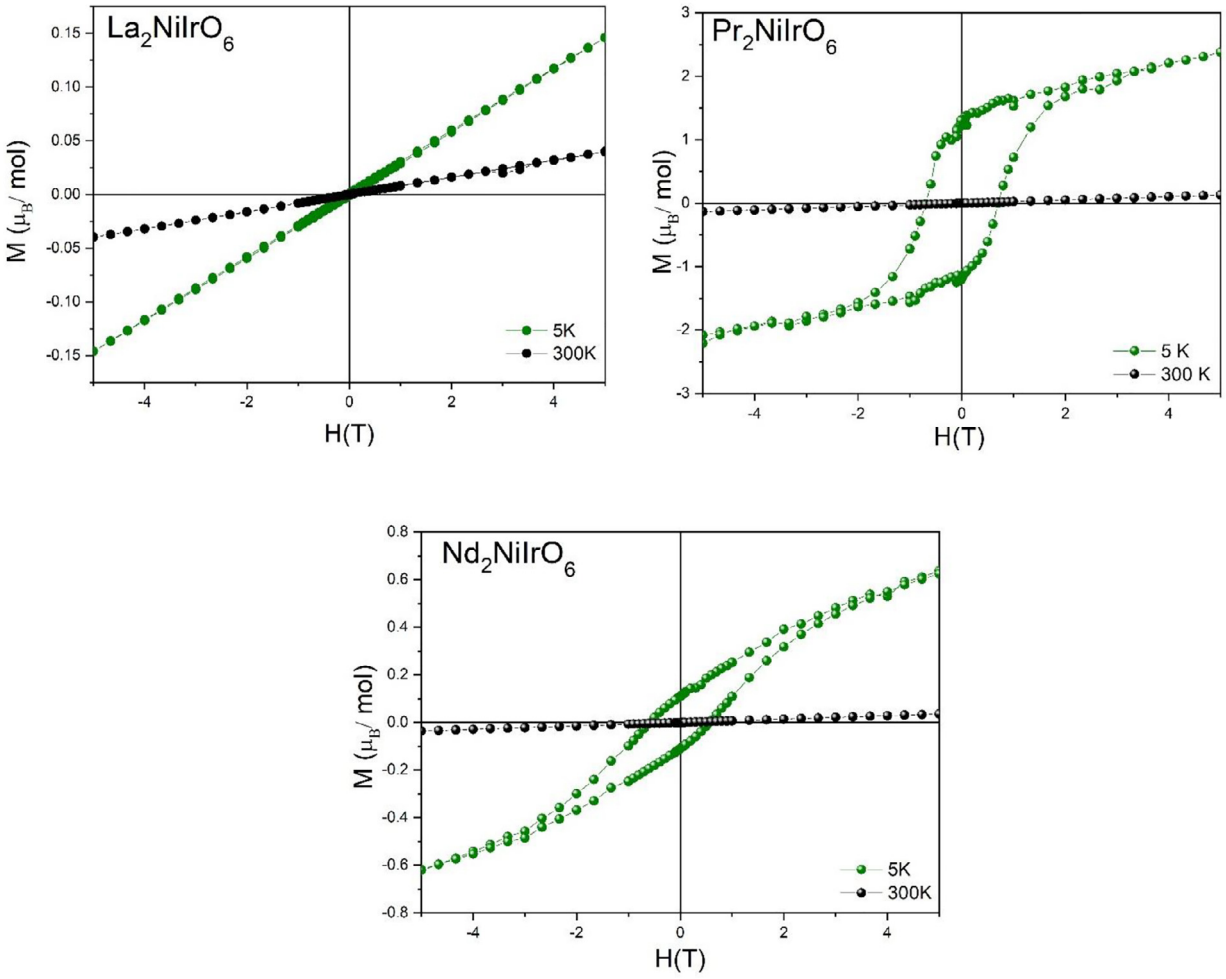


**Fig. 6.** Magnetization versus magnetic field isotherms of $R_2NiIrO_6$ (R = La, Pr, Nd) at 300 K and 4 K measured under a magnetic field ranging from −5 to 5 T.

*Magnetic properties.* dc-susceptibility curves (Fig. 5), measured in both ZFC (zero-field cooled) and FC (field cooled) modes, suggest the existence of antiferromagnetic order at the Néel temperature of 75 K (La), 103 K (Pr) and 121 K (Nd). The divergence between the ZFC and FC curves is ascribed to magnetic irreversibilities, due to magnetic frustration or canting of the spins that allows the presence of weak ferromagnetic components of the magnetic moment in an antiferromagnetic matrix.[10] Another feature observed in the susceptibility curves is the presence of the so-called paramagnetic tail at 30 K in the $Pr_2NiIrO_6$ and $Nd_2NiIrO_6$ perovskites. It has been previously observed in other Ir-based perovskites [3], and it is attributed to imperfections in the long-range ordering of the antiferromagnetic material, which may leave some isolated areas of non-ordered atoms that follow the usual thermal dependence of paramagnetic substances.

Above the magnetic ordering temperature, the reciprocal susceptibility follows the Curie- Weiss law $\chi = C/(T - \theta_W)$. The Weiss temperature and the effective magnetic moments were obtained from the fitting. The latter parameter was estimated from the Curie constant as $2.84\sqrt{C}$. For R= La, Pr and Nd, the determined values are 3.85, 6.22 and 6.33 $\mu_B$/f.u. and the theoretical ones, considering spin-only magnetic moments for $Ni^{2+}$ and $Ir^{4+}$ ions, are 3.30, 5.96 and 6.10 $\mu_B$, respectively, estimated as $\mu_{eff} = (2\mu(R^{3+})^2+\mu(Ni^{2+})^2+\mu(Ir^{4+})^2)^{1/2}$. The J-values for the $Pr^{3+}$ and $Nd^{3+}$cations have been used in this calculation ($^3H_4$ for $Pr^{3+}$; $^4I_{9/2}$ for $Nd^{3+}$; yielding 3.58 and 3.62 $\mu_B$, respectively). The higher value of the effective magnetic moments compared to the theoretical ones is ascribed to a small orbital contribution of $Ni^{2+}$ and $Ir^{4+}$ to the magnetic moment. All the samples display negative Weiss temperature ($\theta_W$ = -51 K, -36 K and -37 K for La, Pr and Nd, respectively), confirming that the dominant interactions are antiferromagnetic in nature. From those values, we can estimate the frustration index, defined as $f_{frus} = |\theta_W|/T_N$ [26]. Since geometrically frustrated materials exhibit $f_{frus} > 10$ we can affirm that these are non-frustrated materials, with $f_{frus}$= 0.68, 0.34 and 0.30 for R= La, Pr and Nd, respectively.

It is worth commenting the unusual behaviour observed concerning the evolution of the antiferromagnetic (AFM) ordering temperature, $T_N$, which evolves from 75 K for R= La to 121 K for R= Nd. Normally, an opposite trend is observed in many series of $ABO_3$ perovskites containing rare-earths at the A position. The reduction in size of $R^{3+}$ ions, according to the lanthanide contraction, implies a decrease of the tolerance factor, involving narrower B-O-B angles and weaker superexchange AFM interactions, which are mediated through the B-O-B chemical bonds. The observed behaviour in the present series may be a consequence of competitive ferromagnetic and antiferromagnetic interactions. This complex magnetic behaviour is intermediate between an ideal collinear arrangement Ir-O-Ni of 180° (ferromagnetic), or an arrangement Ir-O-O-Ir and Ni-O-O-Ni of 90° (antiferromagnetic). Since the Ir-O-Ni bond angle is ~ 150°, the antiparallel coupling is presumed to be dominant over ferromagnetic one.[9,27,28] In this scenario, as the rare-earth ion radius decreases from $La^{3+}$ to $Nd^{3+}$, the Ir-O-Ni angle deviates more from the ideal value (180°) and therefore, the

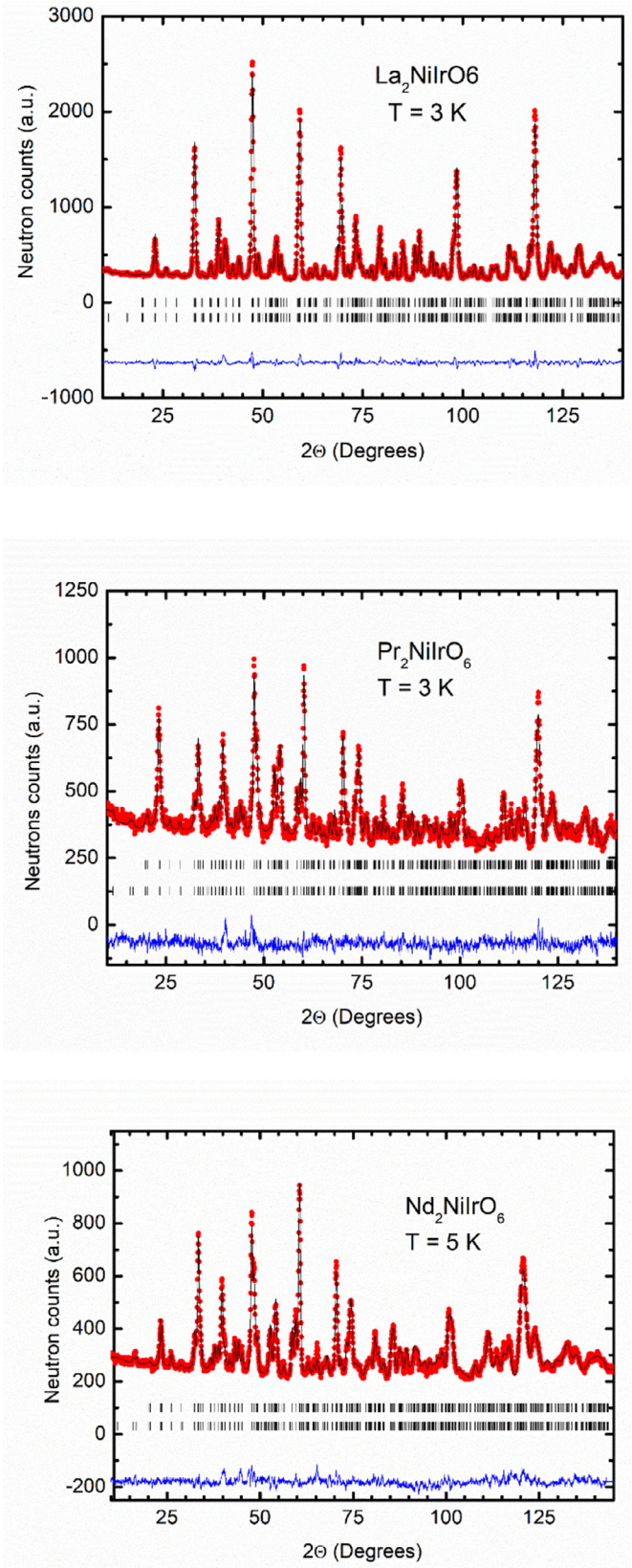


**Fig. 7.** Observed (red circles), calculated (solid black line), and difference (blue line) NPD Rietveld profiles for $R_2NiIrO_6$ at 3 K (La and Pr) and 5 K (Nd). The first series of Bragg reflections corresponds to the main perovskite phase and the second one to the magnetic structure.

possible ferromagnetic interactions are weakening. This results in a predominance of the antiferromagnetic interactions, which leads to an increase in the temperature of the magnetic order ($T_N$).

M/H isotherm curves were measured at 300 K and 4 K between 5 T and -5 T, as shown in Fig. 6. The R= La compound shows a linear behaviour at both temperatures, confirming that antiferromagnetic interactions are predominant. For R= Pr and Nd, there is a noticeable hysteresis loop at 4 K with a non- saturated value of magnetization of 2.36 and 0.62 $\mu_B$/f.u.

*Magnetic structure.* In the neutron diffraction patterns acquired at 3 K and 5 K for $La_2NiIrO_6$ and $Nd_2NiIrO_6$, respectively, new Bragg reflections forbidden by the monoclinic space group $P2_1/n$ are observed, in particular the reflections (1,0,0) and (0,1,0). In the case of $Pr_2NiIrO_6$, a notable increase of the intensity is observed at 3 K for the (0,1,1) and (1,0,1) reflections. For the three compounds, all these Bragg reflections are magnetic in origin, implying that the magnetic order is characterized by the propagation vector k = (0,0,0). The possible magnetic structures compatible with the space group $P2_1/n$ have been obtained by using the representation analysis technique described by Bertaut [29]. In this case, the solutions have been determined by using one of the programs of the Fullprof suite package [17]. For $\mathbf{k} = (0,0,0)$ the small group $G_\mathbf{k}$ coincides with the space group $P2_1/n$ whose irreducible representations are given in Table S3.

The R (La, Pr, Nd) atoms occupy the 4*e* site and they are denoted as 1 (x,y,z), 2 (-x+1/2,y+1/2,-z+1/2), 3 (-x,-y,-z) and 4 (x+1/2,-y+1/2,z+1/2). The notation for the Ni atoms at the 2*b* site is 5 (0,0,1/2) and 6 (1/2,1/2,0) and for the Ir atoms at the 2*a* site is 7 (0,0,0) and 8 (1/2,1/2,1/2). The basis vectors corresponding to each irreducible representation are shown in Table 3. According to Table 3, only the irreducible representations $\Gamma_1$ and $\Gamma_3$ present basis vectors for all the sites. In principle, the magnetic transition observed at $T_N$ for all the compounds is a second order one, so it is expected that all the magnetic atoms order according to the basis vectors belonging to the same irreducible representations.

For $Nd_2NiIrO_6$, after checking the different solutions, the magnetic structure that shows the best agreement with the experimental NPD data acquired at 5 K, corresponds to the basis vectors of the irreducible representations $\Gamma_1$. The refined parameters are listed in Table 4. The experimental and calculated NPD patterns are compared in Fig. 7. For the Nd atoms, the coupling along the *a* and *c* axis is antiferromagnetic, whereas the magnetic moments are ferromagnetically coupled along the *b*-axis. The Ni atoms are ferromagnetically coupled along the *b*-axis and the Ir atoms are antiferromagnetically coupled along the *c*-axis. This scenario implies the presence of both antiferromagnetic and ferromagnetic exchange interactions, what is in good agreement with the results observed in the magnetic measurements, since the susceptibility curves exhibit irreversibilities between FC and ZFC curves, characteristic of competitive interactions, with a negative Weiss temperature and a magnetic hysteresis observed in the magnetization curve measured at 5 K. A plot of the magnetic structure obtained by the VESTA software [30] is displayed in Fig. 8. Let us point out that in the susceptibility curve of Fig. 5, an anomaly is observed around 50 K, what would be associated with the appearance of the magnetic ordering of the Nd moments. The Nd atoms exhibit a ferromagnetic component along the *b*-axis, what would explain the increase of the susceptibility at low temperatures.

Regarding the magnetic structure of the $Pr_2NiIrO_6$ and $La_2NiIrO_6$ perovskites, in both cases the best agreement is also obtained for the magnetic structure given by the basis vectors of the irreducible representation $\Gamma_1$. In both compounds, the magnetic reflections are weak and the fitting factor $R_{Mag}$ is high. A view of the magnetic structures is given in Fig. 8b and c. According to the results displayed in Table 4 for $Pr_2NiIrO_6$, both Pr and Ir atoms only exhibit antiferromagnetic interactions. However, Ni atoms are fer-

**Table 3**
Basis vectors associated with each of the irreducible representations

| | R(Nd, Pr) | | | | | | | | Ni | | | | Ir | | | |
|---|---|---|---|---|---|---|---|---|---|---|---|---|---|---|---|---|
| | 1 | | | 2 | | | 3 | | | 4 | | | 5 | | | 6 | | | 7 | | | 8 | | |
| $\Gamma_1$ | [100] | [010] | [001] | [$\bar{1}$00] | [010] | [00$\bar{1}$] | [100] | [010] | [001] | [$\bar{1}$00] | [010] | [00$\bar{1}$] | [100] | [010] | [001] | [$\bar{1}$00] | [010] | [00$\bar{1}$] | [100] | [010] | [001] | [$\bar{1}$00] | [010] | [00$\bar{1}$] |
| $\Gamma_2$ | [100] | [010] | [001] | [$\bar{1}$00] | [010] | [00$\bar{1}$] | [$\bar{1}$00] | [0$\bar{1}$0] | [00$\bar{1}$] | [100] | [0$\bar{1}$0] | [001] | | | | | | | | | | | | |
| $\Gamma_3$ | [100] | [010] | [001] | [100] | [0$\bar{1}$0] | [001] | [100] | [010] | [001] | [100] | [0$\bar{1}$0] | [001] | [100] | [010] | [001] | [100] | [0$\bar{1}$0] | [001] | [100] | [010] | [001] | [100] | [0$\bar{1}$0] | [001] |
| $\Gamma_4$ | [100] | [010] | [001] | [100] | [0$\bar{1}$0] | [001] | [$\bar{1}$00] | [0$\bar{1}$0] | [00$\bar{1}$] | [$\bar{1}$00] | [010] | [00$\bar{1}$] | | | | | | | | | | | | |

**Table 4**
Results of the fitting of the magnetic structures from the NPD patterns acquired for $Nd_2NiIrO_6$ (T = 5 K), $Pr_2NiIrO_6$ (T = 3 K) and $La_2NiIrO_6$ (T = 3 K).

| Atom | | $Nd_2NiIrO_6$ | $Pr_2NiIrO_6$ | $La_2NiIrO_6$ |
|---|---|---|---|---|
| R | $m_x$, $m_y$, $m_z$ ($\mu_B$) | 0.98(10), 0.4(2), 0.38(14) | 0.93(13), 0, 0 | - |
| | $\|\mathbf{m}\|$ ($\mu_B$) | 1.1(3) | 0.93(13) | - |
| Ni | $m_x$, $m_y$, $m_z$ ($\mu_B$) | 0, 1.4(2), 0 | 0, 2.30(12), 0 | 1.25(12), 0, 0.8(4) |
| | $\|\mathbf{m}\|$ ($\mu_B$) | 1.4(2) | 2.30(12) | 1.5(4) |
| Ir | $m_x$, $m_y$, $m_z$ ($\mu_B$) | 0, 0, 1.6(2) | 1.3(2), 0, 1.6(2) | 0.29(13), 0, -0.6(5) |
| | $\|\mathbf{m}\|$ ($\mu_B$) | 1.6(2) | 2.1(6) | 0.7(5) |
| | $R_{Bragg}$(%) | 9.8 | 11.3 | 2.7 |
| | $R_{Mag}$(%) | 16.0 | 23.1 | 33.3 |
| | $\chi^2$ | 2.8 | 1.6 | 3.4 |

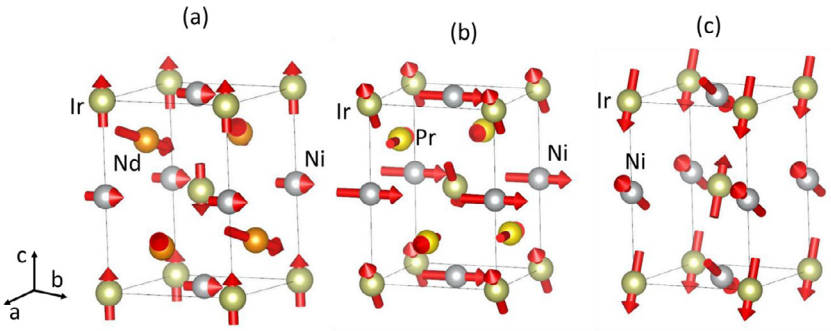


**Fig. 8.** Schematic view of the magnetic structures of (a) $Nd_2NiIrO_6$, (b) $Pr_2NiIrO_6$ and (c) $La_2NiIrO_6$ below $T_N$.

romagnetically coupled along the *b*-axis. For $La_2NiIrO_6$, the magnetic moments are oriented in the *ac* plane, and both atoms exhibit an antiferromagnetic structure, what is in good agreement with the magnetic measurements, as in this case a magnetic hysteresis is not observed in the magnetization curve measured at 5 K. The fact that Ir moment is much smaller in the La compound (0.7(5) $\mu_B$ *vs* 1.6(2) and 2.1(6) $\mu_B$ for Nd and Pr, respectively) can be explained by a higher covalent character of the Ir-O bonds in $La_2NiIrO_6$, induced by the more basic character of La *vs* Nd and Pr. That means a higher delocalization of the valence electrons and a reduction of the magnetic moment.

It is noteworthy mentioning the difference in the arrangement of the magnetic moments for Ni and Ir in the three members of the $R_2NiIrO_6$ family. The rotation of the magnetic moments with respect to the intrinsic magnetic structure of this double perovskites is triggered by the difference in their magnetic anisotropy, strongly influenced by the nature of the rare earth. This feature has been previously reported in similar families of doubles perovskites such as $R_2NiMnO_6$ [31] and $R_2NiRuO_6$ [21]. As it is observed, the spin structure of $La_2NiIrO_6$ ($La^{3+}$ is paramagnetic), is considered as the intrinsic magnetic structure for these series of double perovskites. Here, the magnetic moments are contained within the *ac* plane, and both Ni and Ir magnetic sublattices experience an independent AFM ordering compatible with $\mathbf{k} = 0$, with a non-collinear arrangement between Ni and Ir moments. For $Pr_2NiIrO_6$ and $Nd_2NiIrO_6$ the Ni spins are ferromagnetically coupled, parallel to the *b* direction, while Ir moments are still within the *ac* plane. In particular, the Nd perovskite exhibits a collinear AFM arrangement of Ir moments along the *c* axis. The knowledge of such a variety of microscopic arrangements is essential to understand the magnetic properties described in Figs. 5 and 6, including the hysteresis cycles observed for Pr and Nd, arising from the FM coupling of Ni spins, and the presence of a strong divergence between ZFC and FC curves.

## 4. Conclusions

In summary, we have prepared three member of the $R_2NiIrO_6$ family (R= La, Pr and Nd); the samples are pure and well crystallized. The outcome of the refinement, combining SXRPD and NPD data, results in B-cation ordered double perovskites with small percentage of antisite of the $Ni^{2+}$ and $Ir^{5+}$ cations that slightly increases along the series. The evolution of the unit-cell parameters scales with the size of the rare-earth ion, as well as their thermal evolution in the 300- 1263 K temperature range. The monoclinic symmetry and the $P2_1/n$ space group persists in the mentioned temperature interval. This has been confirmed by analysing the superlattice reflections. Magnetization measurements confirm the existence of antiferromagnetic order at the Néel temperature of 75 K (La), 103 K (Pr) and 121 K (Nd) and the uncommon increase of the magnetic ordering temperature when the size of $R^{3+}$ decreases is ascribed to the competition of ferromagnetic and an-

tiferromagnetic interactions. While the magnetic structures of the three samples are defined by the same propagation vector, $\mathbf{k} = 0$, a substantial difference in the arrangement of the magnetic moments for Ni and Ir is observed, which is explained in terms of the anisotropy of the rare-earth ion.

## Declaration of Competing Interest

The authors declare that they have no known competing financial interests or personal relationships that could have appeared to influence the work reported in this paper.

## Acknowledgements

We thank the financial support of the Spanish Ministry of Economy and Competitiveness to the project MAT2017-84496-R and of EPSRC. We are grateful to the Institut Laue-Langevin and ALBA cells synchrotron (proposal ID 201702206) for making all facilities available.

## Supplementary materials

Supplementary material associated with this article can be found, in the online version, at doi:10.1016/j.actamat.2021.116684.

## References

[1] M.A. Laguna-Marco, P. Kayser, J.A. Alonso, M.J. Martínez-Lope, M. van Veenendaal, Y. Choi, D. Haskel, Electronic structure, local magnetism, and spin-orbit effects of Ir(IV)-, Ir(V)-, and Ir(VI)-based compounds, Phys. Rev. B 91 (2015) 214433.
[2] P. Kayser, B.J. Kennedy, B. Ranjbar, J.A. Kimpton, M. Avdeev, Spin–orbit coupling controlled ground state in the Ir(V) perovskites A2ScIrO6 (A = Ba or Sr), Inorg. Chem. 56 (2017) 2204–2209.
[3] P. Kayser, M.J. Martínez-Lope, J.A. Alonso, M. Retuerto, M. Croft, A. Ignatov, M.T. Fernández-Díaz, Crystal structure, phase transitions, and magnetic properties of iridium perovskites Sr2MIrO6 (M = Ni, Zn), Inorg. Chem. 52 (2013) 11013–11022.
[4] K.I. Kobayashi, T. Kimura, Y. Tomioka, H. Sawada, K. Terakura, Y. Tokura, Intergrain tunneling magnetoresistance in polycrystals of the ordered double perovskite Sr2FeReO6, Phys. Rev. B 59 (1999) 11159–11162.
[5] M. Retuerto, J.A. Alonso, M.J. Martínez-Lope, J.L. Martínez, M. García-Hernández, Record saturation magnetization, Curie temperature, and magnetoresistance in Sr2FeMoO6 double perovskite synthesized by wet-chemistry techniques, Appl. Phys. Lett. 85 (2004) 266–268.
[6] Y. Krockenberger, K. Mogare, M. Reehuis, M. Tovar, M. Jansen, G. Vaitheeswaran, V. Kanchana, F. Bultmark, A. Delin, F. Wilhelm, A. Rogalev, A. Winkler, L. Alff, Erratum: Sr2CrOsO6: end point of a spin-polarized metal-insulator transition by 5d band filling, Phys. Rev. B 75 (2007) 179901.
[7] H. Kato, T. Okuda, Y. Okimoto, Y. Tomioka, Y. Takenoya, A. Ohkubo, M. Kawasaki, Y. Tokura, Metallic ordered double-perovskite Sr2CrReO6 with maximal Curie temperature of 635 K, Appl. Phys. Lett. 81 (2002) 328–330.
[8] H.L. Feng, Z. Deng, M. Wu, M. Croft, S.H. Lapidus, S. Liu, T.A. Tyson, B.D. Ravel, N.F. Quackenbush, C.E. Frank, C. Jin, M.-R. Li, D. Walker, M. Greenblatt, High–pressure synthesis of Lu2NiIrO6 with ferrimagnetism and large coercivity, Inorg. Chem. 58 (2019) 397–404.
[9] R.C. Currie, J.F. Vente, E. Frikkee, D.J.W. Ijdo, The structure and magnetic properties of La2MIrO6 with M = Mg, Co, Ni, and Zn, J. Solid State Chem. 116 (1995) 199–204.
[10] A.V. Powell, J.G. Gore, P.D. Battle, The magnetic properties of iridium in mixed-metal oxides, J. Alloys Compd. 201 (1993) 73–84.
[11] T.D. Rao, S. Marik, D. Singh, R.P. Singh, Observation of exchange bias effect in La2NiIrO6, J. Alloys Compd. 705 (2017) 849–852.
[12] T. Ferreira, G. Morrison, J. Yeon, H.-C. zur Loye, Design and crystal growth of magnetic double perovskite iridates: Ln2MIrO6 (Ln = La, Pr, Nd, Sm-Gd; M = Mg, Ni), Cryst. Growth Des. 16 (2016) 2795–2803.
[13] S.V. Haritha, Investigation of some 4d and 5d transition metal based Double Perovskites Ph. D. Thesis, IISER Pune, India, 2020.
[14] Safdar Nazir, Ferri-magnetic mott-insulating state in Lu2NiIrO6: ab-initio study, J. Alloys Compd. 835 (2020) 155351.
[15] F. Fauth, R. Boer, F. Gil-Ortiz, C. Popescu, O. Vallcorba, I. Peral, D. Fullà, J. Benach, J. Juanhuix, The crystallography stations at the Alba synchrotron, Eur. Phys. J. Plus 130 (2015) 160.
[16] H. Rietveld, A profile refinement method for nuclear and magnetic structures, J. Appl. Crystallogr. 2 (1969) 65–71.
[17] J. Rodríguez-Carvajal, Recent advances in magnetic structure determination by neutron powder diffraction, Physica B 192 (1993) 55–69.
[18] M.T. Anderson, K.B. Greenwood, G.A. Taylor, K.R. Poeppelmeier, B-cation arrangements in double perovskites, Prog. Solid State Chem. 22 (1993) 197–233.
[19] S. Vasala, M. Karppinen, A2B'B"O6 perovskites: a review, Progress Solid State Chem. 43 (2015) 1–36.
[20] M.J. Martínez-Lope, J.A. Alonso, M. Retuerto, M.T. Fernández-Díaz, Evolution of the crystal structure of RVO3 (R = La, Ce, Pr, Nd, Tb, Ho, Er, Tm, Yb, Lu, Y) perovskites from neutron powder diffraction data, Inorg. Chem. 47 (2008) 2634–2640.
[21] P. Kayser, J.A. Alonso, A. Muñoz, M.T. Fernández-Díaz, Structural and magnetic characterization of the double perovskites R2NiRuO6 (R = Pr-Er): a neutron diffraction study, Acta Mater. 126 (2017) 114–123.
[22] A.M. Glazer, The classification of tilted octahedra in perovskites, Acta Crystall. Sect. B 28 (1972) 3384–3392.
[23] R. Shannon, Revised effective ionic radii and systematic studies of interatomic distances in halides and chalcogenides, Acta Crystallogr., Sect. A 32 (1976) 751–767.
[24] I.D. Brown, D. Altermatt, Bond-valence parameters obtained from a systematic analysis of the inorganic crystal structure database, Acta Crystall. Sect. B 41 (4) (1985) 244–247.
[25] C.J. Howard, B.J. Kennedy, P.M. Woodward, Ordered double perovskites – a group-theoretical analysis, Acta Crystall. Sect. B 59 (2003) 463–471.
[26] C.R. Wiebe, J.E. Greedan, G.M. Luke, J.S. Gardner, Spin-glass behavior in the S=1/2 fcc ordered perovskite Sr2CaReO6, Phys. Rev. B 65 (2002) 144413.
[27] J. Wang, K. Li, B. Yu, Z. Wu, Theoretical investigation on the magnetic and electronic properties of La2NiIrO6, Comput. Mater. Sci. 60 (2012) 149–152.
[28] B. John, Goodenough: Magnetism and the Chemical Bond, Interscience Publishers, New York, London, 1963.
[29] E.F. Bertaut, in: G.T.R.A.H. Shul (Ed.), Magnetism, Academic Press, New York, 1963, p. 149.
[30] K. Mommaa, F. Izumi, VESTA 3 for three-dimensional visualization of crystal, volumetric and morphology data, J. Appl. Crystallogr. 44 (2011) 1272–1276.
[31] M. Retuerto, Á. Muñoz, M.J. Martínez-Lope, J.A. Alonso, F.J. Mompeán, M.T. Fernández-Díaz, J. Sánchez-Benítez, Magnetic interactions in the double perovskites R2NiMnO6 (R = Tb, Ho, Er, Tm) investigated by neutron diffraction, Inorg. Chem. 54 (2015) 10890–10900.